POLITECNICO DI TORINO
Repository ISTITUZIONALE

Time-domain parametric models for floating structures: A Loewner-based approach

Original
Time-domain parametric models for floating structures: A Loewner-based approach / Celesti, M.L., Faedo, N.. - In: APPLIED OCEAN RESEARCH. - ISSN 0141-1187. - 166:(2026). [10.1016/j.apor.2025.104876]

Availability:
This version is available at: 11583/3005634 since: 2025-12-04T11:52:02Z

Publisher:
Elsevier

Published
DOI:10.1016/j.apor.2025.104876

Terms of use:

This article is made available under terms and conditions as specified in the corresponding bibliographic description in the repository

Publisher copyright

(Article begins on next page)

25 November 2026

Applied Ocean Research 166 (2026) 104876



Contents lists available at ScienceDirect

Applied Ocean Research

journal homepage: www.elsevier.com/locate/apor



Research paper

Time-domain parametric models for floating structures: A Loewner-based approach

Maria Luisa Celesti *, Nicolás Faedo

Marine Offshore Renewable Energy Lab, Department of Mechanical and Aerospace Engineering, Politecnico di Torino, Turin, Italy

ARTICLE INFO

Keywords:
Offshore floating structures
Parametric hydrodynamic models
Time-domain modelling
Reduced-order models
Loewner framework

ABSTRACT

Design, control, and optimisation of offshore floating structures have undergone significant evolution in recent years, driven by cutting-edge technology, including novel marine renewable energy sources and autonomous underwater vehicles. A key cornerstone is the availability of mathematical models capable of providing an accurate (yet computationally tractable) prediction of their behaviour, under different ocean conditions. The most widely adopted approach for capturing fluid–structure interactions is based on linear potential flow theory, where the system's hydrodynamic behaviour is described through a finite set of frequency-dependent linear coefficients. A well-known limitation of this frequency-domain approach is its inherently non-parametric nature: if not parameterised accordingly, effective time-domain simulation necessitates the numerical solution of a convolution operator, which describes memory effects due to the surrounding fluid, an approach inconvenient for both simulation (computational) and control design (representational compatibility). Not only is a closed-form expression fundamental, but any candidate parametric model also needs to comply with the physical properties characterising a floating structure, including input/output stability, minimum-phase behaviour, and passivity. This paper presents a novel approach to producing physically consistent parametric structures for time-domain modelling of floating systems, utilising a Loewner-based method. The models, capable of providing approximate interpolation of raw frequency-domain data computed with off-the-shelf hydrodynamic solvers, accurately capture the complex behaviour of multi-mode and multi-body offshore structures, while respecting the dynamical properties associated with the system's physics. The technique is illustrated in detail, using four different offshore structures from various fields of ocean engineering, highlighting the benefits of the proposed time-domain modelling framework.

1. Introduction

Offshore floating structures have been historically central to a vast range of traditional maritime industries and related applications, serving critical roles in transportation, resource extraction, and even national defence (Fossen, 2011; Wilson, 2003; Lee and Roh, 2018). Though widely recognised as a well-established field, this is, to date, a rapidly evolving landscape, with the past decade seeing a significant evolution in floating offshore technology, due to *e.g.* the massive boost in interest for marine renewable energies (Otter et al., 2022; Falnes and Kurniawan, 2020; IRENA, 2020) in the path towards global decarbonisation, and the development of novel autonomous underwater vehicles (Sahoo et al., 2019; Zereik et al., 2018), among others.

A key cornerstone in the design, optimisation, operation, and control of offshore structures is the availability of mathematical models capable of providing an accurate (yet computationally tractable) prediction of their behaviour, under a variety of ocean conditions. Regardless of the specific offshore application, the most widely adopted approach for capturing fluid–structure interactions (*i.e.* dynamical response due to the action of ocean waves) is based on the so-called linear potential flow theory (Kundu et al., 2024; Falnes and Kurniawan, 2020; White, 2011), where the hydrodynamic behaviour of the overall system is described through a set of frequency-dependent linear coefficients. These hydrodynamic coefficients are commonly computed numerically in the frequency domain, for a finite set of frequency components, a choice that offers significant computational advantages. By exploiting linearity and, hence, superposition, the response of the structure can be numerically estimated separately at each frequency, yielding a frequency-response representation in terms of a finite set of points (Faltinsen, 1993; Falnes and Kurniawan, 2020). These coefficients are obtained through so-called boundary element methods (BEMs), readily implemented in both open-source and commercial hydrodynamic solvers (Papillon et al., 2020).

* Corresponding author.
E-mail address: marialuisa.celesti@polito.it (M.L. Celesti).

https://doi.org/10.1016/j.apor.2025.104876
Received 12 August 2025; Received in revised form 7 November 2025; Accepted 27 November 2025
Available online 3 December 2025
0141-1187/© 2025 The Authors. Published by Elsevier Ltd. This is an open access article under the CC BY license (http://creativecommons.org/licenses/by/4.0/).

A well-known limitation of this frequency-domain approach is its inherently non-parametric nature, which complicates its use in a time-domain simulation setup, design optimisation routines, and modern control design and synthesis. In other words, with this methodology, the frequency-domain response of the floating structure is represented in terms of a finite set of complex numbers, each corresponding to a particular frequency, and hence no closed-form expression of the dynamical behaviour of the structure is (initially) available. If not parameterised accordingly in terms of a suitable structure, the effective time-domain simulation of a floating body, formulated leveraging the so-called Cummins' equation (Cummins, 1962), necessitates the numerical solution of a convolution operator when included in the overall input/output dynamics to describe the so-called *radiation* effects, which describe the memory effects due to the action of the surrounding fluid, an approach known to be inconvenient both from simulation (computational) and control design (representational compatibility) perspectives. As a matter of fact, efficient simulation for design and optimisation, and development of control technology for offshore structures, virtually always require compact parametric models, typically in state-space form, to enable system analysis, synthesis, and real-time control implementation (Taghipour et al., 2008; Faedo et al., 2021a, 2023).

Not only does having a closed-form expression become fundamental, but any candidate parametric model needs to comply with the physical properties characterising a floating structure, which translates to compliance with specific dynamical properties, including input/output stability, minimum-phase behaviour, and passivity. The latter, which relates to the dissipative nature of radiation effects, can have a significant impact both for simulation and control purposes, and is known to be notoriously difficult to enforce (Perez and Fossen, 2011). As has been previously shown in the literature, see *e.g.* (Faedo et al., 2021a; Taghipour et al., 2008; Unneland and Egeland, 2006), even 'small' violations of passivity can lead to undesired instabilities in the overall input–output model, compromising the role of the parametric representation for numerical simulation purposes. Furthermore, passivity is intrinsically connected with energy-based control, which is the golden standard objective in the ocean renewable energy field (Ringwood et al., 2023): a non-passive model can lead to ill-posed optimal control problems, losing guarantees of existence and uniqueness of control solutions, hence compromising real-time implementation and overall system performance.

Due to its significance and relevance in the ocean engineering field, parametric modelling of offshore floating structures for time-domain simulation and control/estimation purposes has been addressed in the literature using a variety of methods (see *e.g.* (Armesto et al., 2015)) according to the specific application scope, directly exploiting BEM data. Earlier studies (see the comparison paper provided in Peña-Sanchez et al. (2019)) focus on methods based on identifying the impulse response directly, predominantly based on the so-called Prony's method (which essentially decomposes the radiation kernel into a weighted sum of complex exponentials). More contemporary approaches moved away from these formulations, focusing either on input/output representations, *i.e.* transfer functions, or state-space formulations. For instance, a well-established method is that proposed in Taghipour et al. (2008) and implemented in the open-source toolbox (Perez and Fossen, 2009), in which the coefficients of a proposed structure in transfer function form are computed via least squares procedures. This technique, though simple to implement, does not inherently guarantee any of the physical properties discussed within this section. An alternative route is that proposed in Faedo et al. (2020, 2018a), in which so-called model reduction by moment-matching (Astolfi et al., 2020) is exploited to produce parametric forms for radiation forces in terms of a state-space representation. The technique leverages the time-domain definition of moments, initially proposed in Astolfi (2010), and provides an approximating parametric form based on non-convex optimisation, with guarantees of internal stability. Minimum-phase behaviour and/or passivity are not guaranteed, though the authors have proposed a variant for single-input single-output systems in Faedo et al. (2018b), adding a nonlinear constraint within the numerical optimisation stage. Other methods explored include studies based on Hankel singular value decompositions (Kristiansen et al., 2005), though this inherently requires mapping the original frequency domain data into the time domain. In particular, Kristiansen et al. (2005) proposes a two-stage parameterisation, in which a high-order model is obtained for each mode of motion based on Hankel decompositions, and then a model reduction procedure is applied to reduce the overall model complexity. Note that neither minimum-phase nor passive behaviour is guaranteed within Kristiansen et al. (2005). What we believe is a step in the right direction has been taken in Husain et al. (2023), where a passivity index is introduced to 'measure' compliance of parametric models with this paramount physical property. Nonetheless, not only (Husain et al., 2023) is solely based on 'correcting' the output of the methods described above (via non-convex optimisation), but does not guarantee passivity per-se.

Apart from the current limitations described above, very often, the studies proposing new methods for parameterisation numerically illustrate techniques based on either single DoF systems, or very simple geometries (*e.g.* floating cylinders/spheres), which present a relatively simple dynamical behaviour, typically in terms of single mode responses that can be approximated with low order models. In these scenarios, parameterisation techniques based on non-convex optimisation routines can sometimes be effective, since the overall search space for the system parameters is relatively small, and finding globally optimal solutions can be performed with a reasonable computational expense. Nonetheless, the situation can change drastically when considering either multi-DoF (MIMO) geometrically complex structures and/or multiple bodies in water, where interacting dynamics can play a massive role in the overall behaviour of the system (Celesti et al., 2025; Folley et al., 2012). With the significant boost of interest in cutting-edge marine technology, including *e.g.* offshore renewable energies, the geometrical complexity of floating structures has increased significantly in recent years: novel floating offshore wind platforms, new wave energy conversion mechanisms, and even hybrid concepts, combining wind and wave conversion. Design, operation and optimisation of these structures require a delicate interplay between different modes of motion, in which interactions between DoFs become fundamental to understand the overall behaviour of the floating system, both for simulation and for control/estimation purposes. There is, hence, a substantial need for accurate parametric models for complex marine structures, able to represent potentially high-order behaviour due to the inherent interaction between multiple floating systems in multiple modes of motion, while respecting the physical properties characterising the system response.

This study aims at closing this gap, by contributing with a parameterisation technique for generic marine structures, based on the so-called *Loewner* interpolation framework (Mayo and Antoulas, 2007; Antoulas et al., 2017; Karachalios et al., 2021), with the following main characteristics:

- The technique proposed herein is able to construct parametric models directly from the frequency response data computed by BEMs, by organising it into structured left and right interpolation sets. This is, to the best of our knowledge, the first application of Loewner-based theory within the marine hydrodynamics domain.
- Since Loewner interpolation cannot guarantee internal stability per-se, a stabilisation routine is proposed to enforce this property, with guarantees of optimality in the $\mathcal{RH}_2$ sense, based on simple coordinate transformations.
- Following stabilisation, and given its major role in time-domain simulation, a passivation routine is proposed, via convex semi-definite optimisation. In contrast to Faedo et al. (2021a), which proposes a single output (minimal) perturbation, the technique proposed here introduces an additional degree of freedom, used to guarantee passivity while minimising departure from the target BEM response.

Overall, the proposed Loewner-based technique is able to deliver parametric models compliant with all the required physical properties, being of practical significance, without requiring complex non-convex optimisation routines, and implementable with off-the-shelf numerical tools.

To fully illustrate the capabilities and accuracy of the proposed framework, four case studies are treated in detail, from different offshore application fields, including: a large vessel, an array of wave energy converters, a semi-submersible offshore wind platform, and a hybrid wind-wave energy conversion system. These cases, which cover both multi-DoF and multi-body floating interacting systems, are presented in the time and frequency domains, offering different measures of model quality, aiming to provide a comprehensive assessment of the capabilities offered by the proposed Loewner-based technique.

The remainder of this paper is organised as follows. Section 1.1 introduces the notation used within this study. Section 2 discusses the fundamentals underpinning time- and frequency-domain modelling of floating offshore structures, leveraging Cummins' equation. Section 3 describes the proposed Loewner-based parameterisation strategy, while Section 4 discusses the enforcement of *all* corresponding radiation dynamical properties, guaranteeing a well-posed and representative parameterisation for the time-domain characterisation of a generic offshore floating structure. Section 5 provides a thorough evaluation of the Loewner-based technique, highlighting the performance of the strategy for different multi-DoF and multi-body offshore structures. Finally, Section 6 encompasses the main conclusions of this study.

1.1. Notation

Standard notation is used throughout our study, with any exceptions presented within this section. We define $\mathbb{C}_{>0} := \{s \in \mathbb{C} \,|\, \Re(s) > 0\}$ and, analogously, $\mathbb{C}_{\geq 0}$, $\mathbb{C}_{<0}$ and $\mathbb{C}_{\leq 0}$. The imaginary axis is denoted as $\mathbb{C}^0$. The symbol 0 stands for any zero element, dimensioned according to the context, while $\mathbb{I}_n$ denotes the identity in $\mathbb{C}^{n\times n}$. The spectrum of a matrix, *i.e.* the set of its eigenvalues, is denoted as $\lambda(A) \subset \mathbb{C}$, while the associated resolvent set is defined as $\rho(A) := \mathbb{C}/\lambda(A)$. The standard Kronecker product is denoted with $\otimes$, while the symbol $\oplus$ indicates the direct sum operator over a set of matrices $\{A_i\}_{i\in\mathbb{N}_n}$, *i.e.* $\oplus_{i\in\mathbb{N}_n} A_i := \mathrm{diag}(A_1, \dots, A_n)$. Given a continuous function $f(t)$, $t \in \mathbb{R}$, its Laplace transform (provided it exists) is denoted as $F(s)$, $s = \varsigma + \jmath\omega \in \mathbb{C}$, $\{\varsigma, \omega\} \subset \mathbb{R}$. With some abuse of notation, its Fourier transform is denoted as the restriction of F on $\mathbb{C}^0$, *i.e.* $F(\jmath\omega)$. Finally, the convolution between two functions $\{f, g\}$ (provided it exists) is defined and denoted as $(f * g)(t) = \int_{-\infty}^{t} f(\tau)g(t-\tau)\mathrm{d}\tau$.

2. Hydrodynamic models for floating marine structures

This section outlines the fundamentals of frequency- and time-domain hydrodynamic modelling for floating offshore structures, based on the celebrated framework of *linear potential flow theory* (Falnes and Kurniawan, 2020; White, 2011). In particular, the equation of motion of a generic floating body, in a lumped-parameter form about its centre of mass, can be expressed in terms of the following linear continuous-time Volterra integro-differential system:

$$(I + a_\infty)\ddot{q} + k * \dot{q} + k_{\mathrm{r}} q = f_{\mathrm{e}} + g_{\mathrm{ext}}(q, \dot{q}, t), \tag{1}$$

where $I \in \mathbb{R}^{m\times m}$ is the generalised inertia-mass matrix of the body and $q \in \mathbb{R}^m$ denotes the time-dependent displacement vector associated with the overall structure with respect to the centre of mass, defined in $m \in \mathbb{N}$ degrees-of-freedom (DoFs). The constant matrix $k_{\mathrm{r}} \in \mathbb{R}^{m\times m}$ is the so-called hydrostatic stiffness, and represents linear restoring effects (due to the balance between gravitational and buoyancy forces), while f_{e} represents wave excitation effects, *i.e.* force/torque induced on the wetted surface of the device due to the incoming wave field. The (potentially nonlinear) map g_{ext} denotes other potential effects to be considered within (1), often included to improve the quality of the hydrodynamic model, most typically viscous forces, mooring effects, and nonlinear restoring forces (Ringwood et al., 2023).

Finally, the convolution integral, together with the so-called infinite added-mass asymptote $a_\infty \in \mathbb{R}^{m\times m}$, defines *radiation* forces, accounting for fluid memory effects. This specific representation for radiation is due to Cummins' (Cummins, 1962), hence the overall Eq. (1) is virtually always referred to within the literature as "Cummins' equation". Note that the corresponding convolution operator, with impulse response function $k \in L^2(\mathbb{R}^{m\times m})$, captures the impact that changes in the momentum of the fluid at a particular time have on the motion at subsequent times.

Remark 1. Eq. (1) can be easily extended to account for several (interacting) bodies, using the very same mathematical structure (see Folley, 2016). This includes multi-body devices (such as hybrid energy converters) or even arrays of floating structures, as considered within Section 5.

The map k, which depends solely on the geometry of the floating structure when assuming zero forward speed,[1] defines a corresponding causal linear time-invariant system $k : \dot{q} \mapsto k * \dot{q} = f_{\mathrm{rad}}^{\mathrm{conv}}$ with an associated frequency-response function K, defined in terms of the so-called *hydrodynamic coefficients* as:

$$\mathbb{C}^{m\times m} \ni K(\jmath\omega) = b(\omega) + \jmath\omega\left(a(\omega) - a_\infty\right), \tag{2}$$

with $b(\omega) \in \mathbb{R}^{m\times m}$ the radiation damping, $a(\omega) \in \mathbb{R}^{m\times m}$ the radiation added-mass, and where $a_\infty = \lim_{\omega\to\infty} a(\omega) \in \mathbb{R}^{m\times m}$.

The coefficients characterising the radiation subsystem K in (2) are commonly computed via BEM solvers (Papillon et al., 2020), at a finite set of frequency components within a user-specified (finite) bandwidth, and hence a parametric form for k in (1) is not known a priori. This leads to (at least) two fundamental issues: (a) the user commonly requires a fine frequency grid to reconstruct numerically the impulse response k in the time-domain and with sufficient accuracy and; (b) the convolution needs to be discretised and solved numerically accordingly to the reconstruction performed in (a), which is far from being efficient. Since the mere presence of this convolution term represents an inconvenience both from simulation (computational) and control design (representational compatibility) point of views, the standard procedure adopted (see *e.g.* Faedo et al., 2020) is to compute a parametric form for k in terms of a continuous-time state-space system, able to approximate the value of $f_{\mathrm{rad}}^{\mathrm{conv}}(t)$ in a computationally efficient fashion, being simultaneously compatible with modern control design procedures.

Formally, the core idea is then to find an approximating continuous-time dynamical system

$$\tilde{k} : \begin{cases} \dot{x}(t) = Ax(t) + B\dot{q}(t), \\ y(t) = Cx(t) + D\dot{q}(t) \approx f_{\mathrm{rad}}^{\mathrm{conv}}(t) \end{cases} \equiv (A, B, C, D), \tag{3}$$

where $x(t) \in \mathbb{R}^n$ denotes the state vector of (3), $n \in \mathbb{N}$ is the model order, and $\{A, B, C, D\}$ is conformable for (3). From now on, we will denote the space containing all systems of the form (3) as Σ_n^m and, hence, $\tilde{k} \in \Sigma_n^m$. Note that the input/output behaviour of (3) can be computed straightforwardly in terms of the corresponding transfer function, *i.e.*

$$\mathcal{G}(\tilde{k}) \equiv \tilde{K} : \mathbb{C} \to \mathbb{C}^{m\times m},\ s \mapsto \tilde{K}(s) = C(s\mathbb{I} - A)^{-1}B + D. \tag{4}$$

Before going further with the developments within this paper, we note that any candidate approximating system $\tilde{k}$ for k in (1) (equivalently $\tilde{K}$ for K in (2)) needs to respect the physical properties of radiation forces:

[1] This is a standard modelling assumption also in the case of large vessels, see Fossen (2011) and Perez and Fossen (2011).

(P1) $\tilde{K}$ has to be internally stable in the Lyapunov sense, *i.e.* $\lambda(A) \subset \mathbb{C}_{<0}$ in (3). This automatically implies bounded-input bounded-output (BIBO) stability.
(P2) $\tilde{K}$ has to be minimum-phase, *i.e.* its inverse has to be BIBO stable.
(P3) $\tilde{K}$ has to be passive. This property, together with (P1), is equivalent to positive-realness of its transfer function, *i.e.* the matrix $\tilde{K}(\jmath\omega) + \tilde{K}(\jmath\omega)^\star$ has to be positive semi-definite, $\forall \omega \in \mathbb{R}$.

Note that Property (P3) $\not\Longleftrightarrow$ (P1) $\wedge$ (P2). As a matter of fact, (P3) can have a significant impact both for simulation and control purposes: passivity of $\tilde{K}$ guarantees local stability of the differential Eq. (1), for any physically meaningful descriptions of the forces/torques involved. As has been previously shown in the literature (Faedo et al., 2021a; Taghipour et al., 2008), even 'small' violations of passivity can lead to instability when included in the overall device Eq. (1), compromising the role of the approximating model for numerical simulation purposes. Furthermore, passivity is intrinsically connected with energy-maximising control, which is the standard objective in the wave energy conversion field (Ringwood et al., 2023): a non-passive model can lead to ill-posed optimal control problems, losing guarantees of existence and uniqueness of control solutions, hence compromising real-time implementation.

Remark 2. Though one is normally interested in providing a parametric state-space form to replace the convolution in (1), we note that recovering the equivalent (approximated) hydrodynamic coefficients can be performed straightforwardly using (4), *i.e.*

$$\tilde{b}(\omega) = \Re(\tilde{K}(\jmath\omega)) \text{ and } \tilde{a}(\omega) = \frac{\Im(\tilde{K}(\jmath\omega))}{\omega} + a_\infty, \tag{5}$$

for $\omega \in \mathbb{R}/\{0\}$. Note that the value for the added mass at 'infinity frequency' is readily available as an output from BEM codes (see also Zabala et al., 2024).

3. Approximate parametric interpolants in the Loewner framework

This section introduces the fundamentals underpinning the so-called Loewner framework (Antoulas et al., 2017; Karachalios et al., 2021), in which we explicitly derive an (approximate) parametric interpolant for the radiation subsystem data described in Section 2, computed via BEM solvers. To achieve such an objective, we begin by specifying the I/O response to be parameterised, *i.e.* $K(\jmath\omega)$ in (2), by means of two key groups of data. In particular, we define a set of *left interpolation frequencies* $\mathscr{F}_\ell = \{\pm\jmath\mu_i\}_{i\in\mathbb{N}_q} \subset \mathbb{C}^0$, each associated with a corresponding set of m *left tangential directions* and m *left tangential responses*, *i.e.*

$$\jmath\mu_i \rightarrow \{(l_{ij}, v_{ij})\}_{j\in\mathbb{N}_m}, \quad -\jmath\mu_i \rightarrow \{(l_{ij}, \overline{v_{ij}})\}_{j\in\mathbb{N}_m}, \tag{6}$$

for all $i \in \mathbb{N}_q$. Analogously, we define a set of *right interpolation frequencies* $\mathscr{F}_r = \{\pm\jmath\lambda_i\}_{i\in\mathbb{N}_k} \subset \mathbb{C}$, with a corresponding set of m *right tangential directions* and m *right tangential responses*, *i.e.*

$$\jmath\lambda_i \rightarrow \{(r_{ij}, w_{ij})\}_{j\in\mathbb{N}_m}, \quad -\jmath\lambda_i \rightarrow \{(r_{ij}, \overline{w_{ij}})\}_{j\in\mathbb{N}_m}, \tag{7}$$

for all $i \in \mathbb{N}_k$. Some useful remarks are in order, as provided below.

Remark 3. Note that we choose mq and mk left and right tangential directions in total, respectively, in order to guarantee exploring all the elements characterising the target response matrix K. The choice of these directions (and associated responses) is discussed in detail in the following paragraphs.

Remark 4. We assume, from now on, that the sets of left and right interpolation frequencies are disjoint, *i.e.* $\mathscr{F}_\ell \cap \mathscr{F}_r = \emptyset$. This technical assumption, which does not imply any loss of generality for our case of interest, is required to guarantee the existence and uniqueness of the proposed approximating system, as detailed in the following paragraphs.

Remark 5. Note that both $\mathscr{F}_\ell$ and $\mathscr{F}_r$ are closed under complex conjugation by construction. This is specifically useful to produce real interpolants from complex data, as detailed within Remark 6.

The objective is then to find a low-order parametric system $\tilde{K}(s)$ able to fulfil (ideally) the tangential interpolating conditions:

$$\begin{aligned} &\ell_{ij}^\mathsf{T}\tilde{K}(\jmath\mu_i) = v_{ij}^\mathsf{T}, \qquad \ell_{ij}^\mathsf{T}\tilde{K}(-\jmath\mu_{ij}) = \overline{v_{ij}}^\mathsf{T}, \\ &\tilde{K}(\jmath\lambda_{ij})r_{ij} = w_{ij}, \qquad \tilde{K}(-\jmath\lambda_{ij})r_{ij} = \overline{w_{ij}}. \end{aligned} \tag{8}$$

Regarding the pairs $\{(\ell_{ij}, v_{ij}), (\ell_{ij}, \overline{v_{ij}})\}$ and $\{(r_{ij}, w_{ij}), (r_{ij}, \overline{w_{ij}})\}$, for each left/right driving frequency in (6)–(7), different choices can be pursued, as long as the directions can fully characterise the underlying function (in line with Remark 3). Within this paper, we use orthogonal canonical directions in $\mathbb{C}^m$, *i.e.*

$$\begin{aligned} &\ell_{ij} = e_j^m, \qquad v_{ij} = \mathrm{row}_j(K(\jmath\mu_i))^\mathsf{T}, \\ &r_{ij} = e_j^m, \qquad w_{ij} = \mathrm{col}_j(K(\jmath\lambda_i)). \end{aligned} \tag{9}$$

Noting that e_j^m are indeed the columns of the identity matrix $\mathbb{I}_m$, and to streamline the exposition and definition of the proposed approximants, we organise the available data in compact form, in terms of the following matrices:

$$\begin{aligned} M &= \bigoplus_{i\in\mathbb{N}_q} \left(\mathbb{I}_m \otimes \begin{bmatrix} \jmath\mu_i & 0 \\ 0 & -\jmath\mu_i \end{bmatrix} \right), \\ L^\mathsf{T} &= \left(\mathbb{1}_q \otimes \mathbb{I}_m\right) \otimes [1\ 1] \\ V^\mathsf{T} &= \sum_{i\in\mathbb{N}_q} e_i^q \otimes \mathfrak{v}_i, \\ \mathfrak{v}_i &= \Big[\mathrm{row}_1(K(\jmath\mu_i))^\mathsf{T} \quad \mathrm{row}_1(\overline{K(\jmath\mu_i)})^\mathsf{T} \quad \dots \\ &\qquad \mathrm{row}_m(K(\jmath\mu_i))^\mathsf{T} \quad \mathrm{row}_m(\overline{K(\jmath\mu_i)})^\mathsf{T} \Big], \end{aligned} \tag{10}$$

for the case of left data, and, analogously,

$$\begin{aligned} \Lambda &= \bigoplus_{i\in\mathbb{N}_k} \left(\mathbb{I}_m \otimes \begin{bmatrix} \jmath\lambda_i & 0 \\ 0 & -\jmath\lambda_i \end{bmatrix} \right), \\ R &= \left(\mathbb{1}_k \otimes \mathbb{I}_m\right) \otimes [1\ 1] \\ W &= \sum_{i\in\mathbb{N}_k} e_i^k \otimes \mathfrak{w}_i, \\ \mathfrak{w}_i &= \Big[\mathrm{col}_1(K(\jmath\lambda_i)) \quad \mathrm{col}_1(\overline{K(\jmath\lambda_i)}) \quad \dots \\ &\qquad \mathrm{col}_m(K(\jmath\lambda_i)) \quad \mathrm{col}_m(\overline{K(\jmath\lambda_i)}) \Big], \end{aligned} \tag{11}$$

for the right interpolation data.

Remark 6 (*Real Interpolants from Complex Data*)**.** To avoid the construction of complex-valued interpolants, since the underlying radiation physical system is effectively defined over $\mathbb{R}$, we consider the change of coordinates defined by the unitary matrix

$$J = \frac{1}{\sqrt{2}} \begin{bmatrix} 1 & \imath \\ 1 & -\imath \end{bmatrix}. \tag{12}$$

Let $J_\gamma = \mathbb{I}_\gamma \otimes J$. Since both $\mathscr{F}_\ell$ and $\mathscr{F}_r$ are closed under complex conjugation (see Remark 5), the associated change of coordinates:

$$\begin{aligned} &\Lambda^\mathbb{R} = J_{km}^\star \Lambda J_{km}, \quad R^\mathbb{R} = R J_{km}, \quad W^\mathbb{R} = W J_{km}, \\ &M^\mathbb{R} = J_{qm}^\star M J_{qm}, \quad L^\mathbb{R} = J_{qm}^\star L, \quad V^\mathbb{R} = J_{qm}^\star V, \end{aligned} \tag{13}$$

transforms the complex data in (10) and (11) into isomorphic real forms.

We are now ready to define two key quantities (Antoulas et al., 2017), which are at the heart of the approximation technique adopted: The Loewner, $\mathbb{L}$, and shifted Loewner, $\mathbb{L}_s$, matrices, for the left and right data in (13). In particular, $\mathbb{L}$ can be defined (Mayo and Antoulas, 2007) as the unique solution of the Sylvester equation

$$M^\mathbb{R}\mathbb{L} - \mathbb{L}\Lambda^\mathbb{R} = V^\mathbb{R}R^\mathbb{R} - L^\mathbb{R}W^\mathbb{R}, \tag{14}$$

where uniqueness follows straightforwardly from the fact that $\mathscr{F}_\ell \cap \mathscr{F}_r = \emptyset$ by construction (see Remark 4). Analogously, the shifted Loewner matrix $\mathbb{L}_s$ satisfies the (shifted) Sylvester equation

$$M^{\mathbb{R}}\mathbb{L}_s - \mathbb{L}_s\Lambda^{\mathbb{R}} = M^{\mathbb{R}}V^{\mathbb{R}}R^{\mathbb{R}} - L^{\mathbb{R}}W^{\mathbb{R}}\Lambda^{\mathbb{R}}. \tag{15}$$

With the left and right data from the target frequency response K in (2), and the associated Loewner and shifted Loewner matrices (solution of (14) and (15), respectively), it is now possible to compute the corresponding approximate parametric interpolants for a generic marine energy conversion system. Let

$$\operatorname{rank}\,\xi\mathbb{L} - \mathbb{L}_s = \operatorname{rank}\begin{bmatrix}\mathbb{L} & \mathbb{L}_s\end{bmatrix} = \operatorname{rank}\begin{bmatrix}\mathbb{L} \\ \mathbb{L}_s\end{bmatrix} = z, \tag{16}$$

for all $\xi \in \mathscr{F}_\ell \cup \mathscr{F}_r$, be the rank associated with the Loewner pencil $(\mathbb{L}, \mathbb{L}_s)$, and consider the thin (often referred to also as 'economic') singular value decompositions (SVDs):

$$\begin{bmatrix}\mathbb{L} & \mathbb{L}_s\end{bmatrix} = Y_1 S_1 X_1^{\mathsf{T}}, \quad \begin{bmatrix}\mathbb{L} \\ \mathbb{L}_s\end{bmatrix} = Y_2 S_2 X_2^{\mathsf{T}}, \tag{17}$$

where $\{S_1, S_2\} \subset \mathbb{R}^{z\times z}$, $Y_1 \in \mathbb{R}^{q\times z}$ and $X_2 \in \mathbb{R}^{k\times z}$. Let $n \le z$ and define the following projected decompositions:

$$Y_1^n = Y_1\begin{bmatrix}\mathbb{I}_n \\ 0\end{bmatrix}, \quad X_2^n = X_2\begin{bmatrix}\mathbb{I}_n \\ 0\end{bmatrix}, \tag{18}$$

The quadruple (E, A, B, C) given (Antoulas et al., 2017) by

$$\begin{aligned} E &= -Y_1^{nT}\mathbb{L}X_2^n, \quad & A &= -Y_1^{nT}\mathbb{L}_s X_2^n, \\ B &= Y_1^{nT}V^{\mathbb{R}}, & C &= W^{\mathbb{R}}X_2^n, \end{aligned} \tag{19}$$

defines an (approximate) interpolant of the data, *i.e.*

$$\tilde{K}(s) : s \mapsto C(sE - A)^{-1}B \approx K(s). \tag{20}$$

Remark 7. If $n = z$, (20) is an *exact* interpolant for the corresponding left and right data with McMillan degree $\nu = \operatorname{rank}\mathbb{L}$.

Remark 8. Complexity (model order) of the data-driven interpolant in (19) is essentially controlled by keeping the largest $n < z$ singular values of the decomposition associated with the Loewner pencil in (16) only, *i.e.* the first n columns of Y_1 and X_2, as per Eq. (19).

It is straightforward to prove that Eq. (20) defines, in fact, the transfer function of an associated continuous-time system (in the form of (3)), written, for all $t \in \mathbb{R}$, as

$$\tilde{k} : \begin{cases} \dot{x}(t) = \underline{A}x(t) + \underline{B}\dot{q}(t), \\ y(t) = Cx(t) \approx f_{\text{rad}}^{\text{conv}}(t) \end{cases} \equiv (\underline{A}, \underline{B}, C, 0), \tag{21}$$

with $x(t) \in \mathbb{R}^n$, and where $\underline{A} = E^{-1}A$ and $\underline{B} = E^{-1}B$.

Remark 9. Given the properties of the radiation system (in particular, causality), it is reasonable to assume that, for every possible model order $n \in \mathbb{N}$, 0 is not an eigenvalue of E, *i.e.*, $0 \notin \lambda(E)$, and hence the matrices $\underline{A}$ and $\underline{B}$ are always well-defined. Nonetheless, if, due to numerical issues, E loses rank, one can simply resort to a generalised inverse instead (see Karachalios et al., 2021).

Remark 10. BEM solvers are known to present noisy components at high frequencies, often induced by so-called 'irregular frequencies'. We note that, to solve this, and before parametrising, post-processing techniques exist and are widely used (see, for instance, Zabala et al., 2024). Nonetheless, we note that, though beyond the scope of this paper, specific choices for the left and right interpolation frequencies $\mathscr{F}_l$ and $\mathscr{F}_r$, respectively, can enhance the robustness of the Loewner-based parameterisation (see the arguments in Kergus and Gosea, 2022).

In order to provide an intuitive overview of the workflow presented in Section 3, Fig. 1 graphically summarises the proposed parametric approximation procedure described in Eqs. (6)–(21). The diagram outlines the main stages of the method, from the BEM data to the construction of the Loewner matrices and the parametric model $\tilde{K}$.

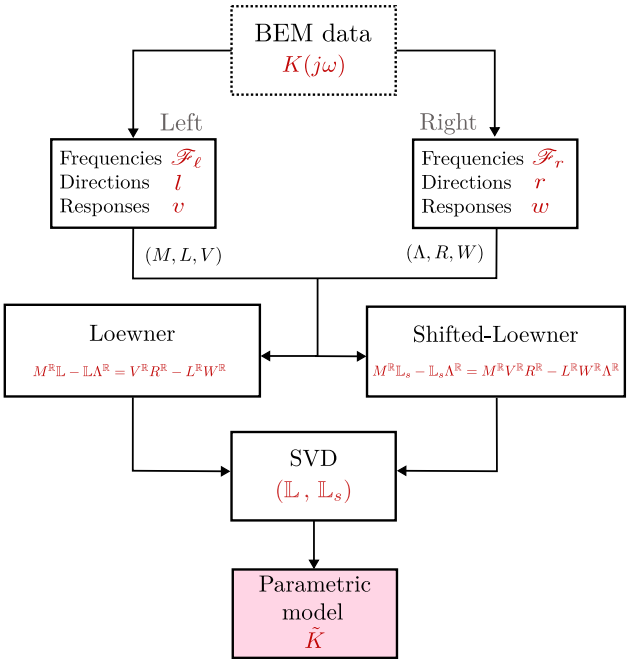

Fig. 1. Schematic representation of the proposed parametric approximation.

4. Enforcing physical properties

The parametric model computed in (21), which is solely based on an SVD and a subsequent projection, is not guaranteed to exhibit the three main properties (P1), (P2) and (P3), as listed within Section 1. This is an inherent limitation of the Loewner-based approach as described within Section 3. As such, in the following, a method to enforce all of these system properties on the parametric Loewner-based model $\tilde{k}$ is proposed, with mild computational requirements. This task is pursued in the following order: (P1) is first explicitly addressed, *i.e.* enforcing stability, which, having now a stable model, facilitates enforcing (P3) in terms of convex optimisation, as demonstrated within this section. Note that compliance with passivity (P3) immediately guarantees minimum-phase behaviour (P2) (see the discussion in Section 1).

Regarding (P1), it is first noted that, while the computed model $\tilde{k}$ in (21) is not necessarily internally stable (as discussed immediately above), this is often the case for reasonable selections of model order n in the corresponding projection (18). In fact, as demonstrated within the diverse case studies presented within Section 5, the presence of a large number of unstable modes, *i.e.* unstable elements in the set $\lambda(\underline{A})$, can be effectively used to infer a reasonable model order for the corresponding radiation parameterisation. Nonetheless, if unstable modes are present for a given desired model order n, an optimal stable approximation $\tilde{k}_{\text{stb}}$ for $\tilde{k}$ is proposed within Section 4.1 to enforce (P1), in a suitable system space.

Finally, once (P1) is guaranteed, (P3) is addressed directly via convex semi-definite optimisation within Section 4.2, in terms of the Kalman–Yakubovich–Popov lemma. In particular, the (now stable) radiation system $\tilde{k}_{\text{stb}}$ is perturbed in terms of its output and feedthrough matrices, in order to guarantee passivity, with minimal intervention.

4.1. Enforcing stability

As outlined above, in the case that $\tilde{k}$ in (21) does not comply with (P1), the underlying idea is to compute a stable approximation in a suitably defined space of systems. Given that $D = 0$ in (21) (*i.e.* $\tilde{k}$ is

strictly proper), the natural choice is to find the closest stable system within the Hardy space $\mathcal{RH}_2$, formally defined as

$$\mathcal{RH}_2 := \left\{ G \in \mathbb{R}(s)^{m\times m} \;\middle|\; \mathbb{C}^0 \subset \mathrm{dom}(G),\ \|G\|_2 < \infty \right\}, \tag{22}$$

that is, the family of strictly proper rational functions which are analytic on $\mathbb{C}_{>0}$. Before describing the stability enforcement procedure, we define the following general class of spaces for state-space systems:

$$\begin{aligned} {}^{0}\Sigma_n^m &:= \left\{(A,B,C,0) \in \Sigma_n^{p,m} |\ \mathbb{C}^0 \subset \rho(A)\right\}, \\ {}^{+}\Sigma_n^m &:= \left\{(A,B,C,0) \in \Sigma_n^{p,m} |\ \mathbb{C}_{\geqslant 0} \subset \rho(A)\right\}, \\ {}^{-}\Sigma_n^m &:= \left\{(A,B,C,0) \in \Sigma_n^{p,m} |\ \mathbb{C}_{\leqslant 0} \subset \rho(A)\right\}, \end{aligned} \tag{23}$$

where ${}^{+}\Sigma_n^m$ and ${}^{-}\Sigma_n^m$ are the sets of the *stable* and *antistable* systems or order n, respectively. We further introduce the following two useful operators between two generic systems Σ_1 and Σ_2:

$$\begin{aligned} \Sigma_1 \amalg \Sigma_2 &:= \left(\begin{bmatrix} A_1 & 0 \\ 0 & A_2 \end{bmatrix}, \begin{bmatrix} B_1 \\ B_2 \end{bmatrix}, \begin{bmatrix} C_1^T \\ C_2^T \end{bmatrix}^T, 0 \right), \\ T_1\Sigma_2 T_2 &:= \left(T_1 A T_2, T_1 B, C T_2, 0\right), \end{aligned} \tag{24}$$

where the matrices T_1, T_2 are conformable. Note that the operator $\amalg$ essentially describes the parallel interconnection between two state-space systems. Furthermore, $\Sigma_1 \sim \Sigma_2$ is used to denote that Σ_1 and Σ_2 are restricted equivalents, *i.e.* there exist regular matrices T_1, T_2 such that $\Sigma_2 = T_1\Sigma_1 T_2$.

We are now ready to introduce the definition of the approximation problem for $\tilde{k}$ in $\mathcal{RH}_2$: Suppose $\tilde{k} \in {}^{0}\Sigma_n^m$. Find $\tilde{k}_{\mathrm{stb}} \in \bigcup_{\hat{n}\in\mathbb{N}} {}^{+}\Sigma_{\hat{n}}^m$ such that

$$\left\|\mathcal{G}(\tilde{k}) - \mathcal{G}(\tilde{k}_{\mathrm{stb}})\right\|_2 = \inf_{\hat{k}\in\bigcup_{\hat{n}\in\mathbb{N}} {}^{+}\Sigma_{\hat{n}}^m} \left\|\mathcal{G}(\Sigma) - \mathcal{G}(\hat{k})\right\|_2. \tag{25}$$

Remark 11. The definition in (25) essentially aims for the computation of the closest (in a 2-norm sense) strictly proper stable system to a given unstable $\tilde{k}$.

To characterise and compute a solution for the approximation problem in (25), we exploit, in the following, a fundamental result from Köhler (2014). Let $\tilde{k} \in {}^{0}\Sigma_n^m$. Then, there exists ${}^{+}\tilde{k} \in {}^{+}\Sigma_n^m$ and ${}^{-}\tilde{k} \in {}^{-}\Sigma_n^m$ such that $\tilde{k} \sim {}^{+}\tilde{k} \amalg {}^{-}\tilde{k}$. Furthermore, ${}^{+}\tilde{k}$ solves (25), *i.e.*

$$\begin{aligned} \inf_{\hat{k}\in\bigcup_{\hat{n}\in\mathbb{N}} {}^{+}\Sigma_{\hat{n}}^m} \left\|\mathcal{G}(\tilde{k}) - \mathcal{G}(\hat{k})\right\|_2 &= \left\|\mathcal{G}(\tilde{k}) - \mathcal{G}({}^{+}\tilde{k})\right\|_2 \\ &= \left\|\mathcal{G}({}^{-}\tilde{k})\right\|_2 \end{aligned} \tag{26}$$

where the solution is unique in the following sense: If $\underline{\tilde{k}}$ is another solution, then it is also a realisation of $\mathcal{G}({}^{+}\tilde{k})$.

This result, which seems somewhat natural, essentially implies that one can always decompose a given unstable system $\tilde{k}$ as a parallel interconnection between stable ${}^{+}\tilde{k}$ and antistable ${}^{-}\tilde{k}$ 'parts'. Furthermore, ${}^{+}\tilde{k}$ represents the optimal stable approximation of $\tilde{k}$ in $\mathcal{RH}_2$, and hence one sets $\tilde{k}_{\mathrm{stb}} = {}^{+}\tilde{k}$ to ensure (P1). In particular, with some abuse of notation,[2]

$$\begin{aligned} \tilde{k} \approx \tilde{k}_{\mathrm{stb}} : &\begin{cases} \dot{x}(t) = \underline{A}_{\mathrm{stb}} x(t) + \underline{B}_{\mathrm{stb}} \dot{q}(t), \\ y(t) = C_{\mathrm{stb}}(t) \end{cases} \\ &\equiv (\underline{A}_{\mathrm{stb}}, \underline{B}_{\mathrm{stb}}, C_{\mathrm{stb}}, 0). \end{aligned} \tag{27}$$

The explicit computation of ${}^{+}k$, as per Eq. (26), can be performed using simple matrix operations to decouple stable and unstable modes, see *e.g.* Bavely and Stewart (1979).

Remark 12. Note that the feedthrough matrix in (27) is effectively 0 as per in (21), since $\tilde{k}_{\mathrm{stb}} \in \mathcal{RH}_2$.

[2] Note that, while we are also using the notation x for the state vector of (27) (to simplify the exposition), this vector is effectively different from that defined within (21).

Remark 13. If $\tilde{k}$ in (21) is already stable, then it is trivial to show that $\tilde{k} = {}^{+}\tilde{k} = \tilde{k}_{\mathrm{stb}}$, since stability of (21) automatically implies that $\tilde{k} \in \mathcal{RH}_2$.

4.2. Enforcing passivity

As discussed within Section 2, one of the main properties of the radiation subsystem k is passivity, *i.e.* (P3). This property, which is related to the dissipative nature of radiation forces, plays a fundamental role in guaranteeing well-posedness of both the simulation of floating structures and their associated model-based control design and synthesis procedures.

To guarantee property (P3) in the resulting parameterisation, a perturbation technique is proposed in the spirit of Faedo et al. (2021a), in which the transmission zeros of the stable system $\tilde{k}_{\mathrm{stb}}$, obtained via Loewner and (if necessary) the stabilisation procedure described in Section 4.1, are modified accordingly, to ultimately enforce passivity. In particular, system (21) is modified in terms of its output and feedthrough matrices, as

$$\begin{aligned} \tilde{k}_{\mathrm{stb}} \approx \tilde{k}_{\mathrm{pas}} : &\begin{cases} \dot{x}(t) = \underline{A}_{\mathrm{stb}} x(t) + \underline{B}_{\mathrm{stb}} \dot{q}(t), \\ y(t) = (C_{\mathrm{stb}} + \Delta C) x(t) + \Delta D \dot{q}(t), \end{cases} \\ &\equiv (\underline{A}_{\mathrm{stb}}, \underline{B}_{\mathrm{stb}}, C_{\mathrm{stb}} + \Delta C, \Delta D), \end{aligned} \tag{28}$$

where the output and feedthrough perturbations ΔC and ΔD are computed as the solution of the convex semi-definite optimisation problem

$$\begin{aligned} &\min_{(\Delta C, \Delta D)} \sum_{i\in\mathbb{N}_{q+k}} \epsilon_i^2 \\ &\text{subject to:} \\ &\epsilon_i = \left\| K(\jmath\omega_i) - (C_{\mathrm{stb}} + \Delta C)(\jmath\omega_i \mathbb{I}_n - \underline{A}_{\mathrm{stb}})^{-1} \underline{B}_{\mathrm{stb}} - \Delta D \right\|_F, \\ &\omega_i \in \mathscr{F}_\ell \cup \mathscr{F}_r, \\ &\begin{bmatrix} P\underline{A}_{\mathrm{stb}} + \underline{A}_{\mathrm{stb}}^{\mathsf{T}} P & P\underline{B}_{\mathrm{stb}} - (C_{\mathrm{stb}} + \Delta C)^{\mathsf{T}} \\ * & -(\Delta D + \Delta D^{\mathsf{T}}) \end{bmatrix} \leq 0, \\ &\|\Delta D\|_F^2 \leq \gamma, \\ &P = P^{\mathsf{T}} > 0. \end{aligned} \tag{29}$$

Some remarks regarding Problem (29) are now in order.

Remark 14. Problem (29) enforces the conditions of the well-known Kalman–Yakubovich–Popov lemma (see, for instance, Marquez (2003, Chapter 8)) via ΔC and ΔD, while minimising the difference between the target frequency response $K(\jmath\omega)$ and that corresponding to $\tilde{k}_{\mathrm{pas}}$, for the set of left and right interpolation frequencies used within Loewner, *i.e.* $\mathscr{F}_\ell \cup \mathscr{F}_r$. This is indeed in contrast to Faedo et al. (2021a), which defines an output perturbation matrix ΔC only, and minimises its associated norm within the cost function (hence not optimising the difference between target and model frequency responses).

Remark 15. Given that $\lambda(A_{\mathrm{st}}) \subset \mathbb{C}_{<0}$, due to the stability of ${}^{+}\tilde{k}$, Problem (29) is always feasible, for γ sufficiently large (see Remark 16). Furthermore, the convexity of (29) follows immediately from applying the canonical vectorisation map $\mathbb{R}^{m\times n} \times \mathbb{R}^{m\times m} \to \mathbb{R}^{mn} \times \mathbb{R}^{m^2}$ to the perturbation matrices (and corresponding objective function).

Remark 16. The parameter $\gamma \in \mathbb{R}^+$ is employed to bound the use of the feedthrough matrix when ensuring passivity, hence minimising the departure of (28) from a strictly proper representation. The selection of this parameter in practical scenarios is treated in detail within Section 5. We further note that it is easy to show that adding a non-zero feedthrough term to the radiation parameterisation does not change the relative degree of the equation of motion (1), which is ultimately the dynamical behaviour of interest.

Remark 17. Problem (29) can be solved using state-of-the-art solvers (see *e.g.* the tools provided within the open-source suite SeDuMi (Sturm, 1999)), which can handle linear matrix inequalities (LMIs) efficiently.

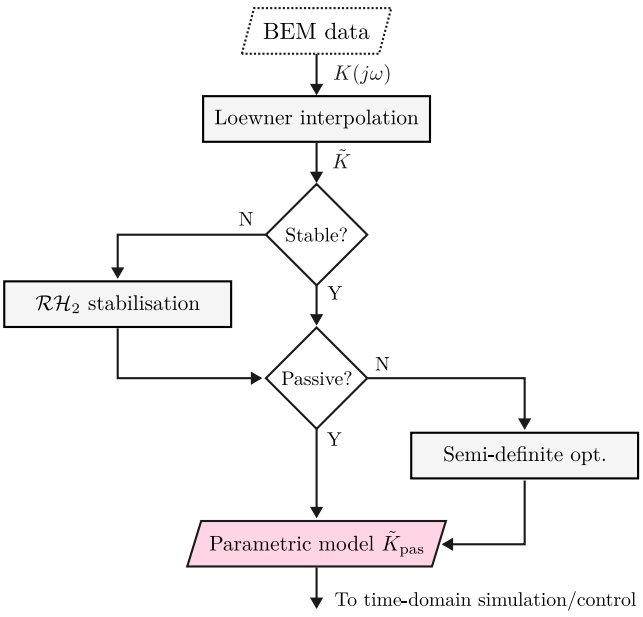

Fig. 2. Algorithmic overview of the proposed time-domain parameterisation procedure.

4.3. Algorithmic overview

To illustrate the overall procedure, Fig. 2 presents an overview of the proposed time-domain parameterisation framework, aiming to offer insight into its use in practical BEM-based scenarios, including, for instance, geometry optimisation loops (Carapellese et al., 2024). The algorithm starts with the user input, *i.e.* the BEM data, together with the left and right frequencies chosen for interpolation (see Section 3) and a desired model order n. A stability check follows: If the computed parametric interpolant $\tilde{K}$ (21) is not stable, then the stabilisation routine proposed in Section 4.1 is executed. Finally, passivity is assessed and, if required, the passivation semi-definite enforcement, proposed within Section 4.2, is considered. Ultimately, the output of the overall procedure is the stable and passive parametric model $\tilde{K}_{\text{pas}}$, as per Eq. (28), ready to be used for time-domain simulation/control/estimation purposes.

4.4. A note on computational complexity

We briefly address, via exhaustive numerical simulation, an estimation of the computational complexity of the proposed procedure, with emphasis on the potentially costly operations, *i.e.* computing the SVD in (17) and the solution to the passivation problem (29). The objective of this brief analysis is that of providing the user with an estimate of the cost of running the proposed parameterisation procedure, information which can be particularly useful for *e.g.* iterative design procedures for offshore structures, in which BEM-data parameterisation can be fundamental for performance evaluation. Note that the stabilisation procedure described in Section 4.1 is not considered, since it essentially requires a single change of coordinates (basis) and one canonical projection (Bavely and Stewart, 1979).

Fig. 3 offers a numerical appraisal of the normalised run time (against the time required to compute the operation for the maximum tested dimension), for the SVD in (17) (left) and the passivation procedure (29) (right).

Starting with the economic SVD, we use the built-in Matlab function "svd" with the "economic" flag active. We keep one dimension fixed (number of columns - n_{col}) and vary the number of rows - n_{rows} - for the Loewner pencil. We run 10^3 tests for each n_{row} considered, to present

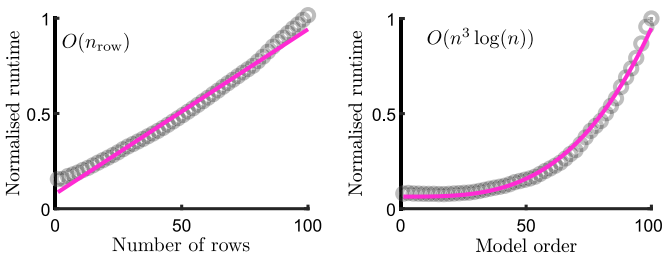

Fig. 3. Numerical estimation of (mean) normalised runtimes for the economic SVD (left) and LMI passivation routine (right). The maximum times, used for normalisation, are 0.0058 [s] and 30 [s], respectively.

mean runtime values. From Fig. 3 (left), we can readily appreciate that the complexity for the economic SVD is approximately linear, *i.e.* $\approx O(n_{\text{row}})$. Furthermore, this behaviour is consistent for any fixed n_{col}, which suggests that the overall complexity is bilinear, *i.e.* $\approx O(nm)$. Regarding the latter, *i.e.* the proposed passivation procedure, the set of LMIs in (29) is solved using MOSEK (interior-point, default settings, see MOSEK ApS, 2025), interfaced via YALMIP (Löfberg, 2004). For the numerical estimation of complexity, we vary the state-space dimension in (28) (*i.e.* the model order - n), while we keep the number of DoF (inputs/outputs) - m - fixed. This is due to the fact that $n \gg m$, so the "dominant" dimension (in terms of complexity) is the order of system (28). As per the SVD case, we run 10^3 tests for each order considered, to provide mean runtime values. From Fig. 3 (right), we can appreciate that the passivation procedure is indeed, as expected, more costly than the SVD, with an estimated complexity of $\approx O(n^3 \log(n))$. Nonetheless, for typical model orders used to parameterise BEM hydrodynamics (see the case studies presented in Table 1), the time required to passivise is in the order of seconds, being 30 [s] the mean runtime for the limit case tested $n = 100$. Note that, up to order $n = 50$, the runtime is hence ≈ 3 [s], being this negligible compared to running a BEM simulation within an optimisation loop itself.

5. Case studies

Aiming to fully illustrate the capabilities of the proposed technique, this section presents four representative case studies, selected to capture a broad spectrum of hydrodynamic behaviour representative of diverse floating marine systems. The considered examples span more conventional marine structures, including a large vessel, and systems arising from the field of ocean renewable energy, comprising an array of wave energy converters (WECs), a floating offshore wind platform, and a hybrid wind–wave energy converter (HWWEC). The different case studies are intended to demonstrate the flexibility, scalability, and robustness of the proposed modelling framework when applied to diverse offshore applications, either in multi-DoF and/or multi-body cases.

A schematic representation of the surface meshes used for the computation of the corresponding hydrodynamic coefficients is shown in Fig. 4. In particular, these correspond to the geometries used as input within the BEM solver, *Capytaine* (Ancellin and Dias, 2019), for computing the hydrodynamic coefficients required for the analysis. An overview of the main geometric properties of each case study, along with the corresponding analysed DoFs, is provided in Table 1. Further details and relevant references providing a technical description for each device are presented in the dedicated subsections (see Sections 5.1–5.4), where specific analyses are performed in both the frequency and time domains, providing a comprehensive numerical appraisal of the theoretical framework proposed within our study.

In order to provide a consistent evaluation of model performance and to quantitatively assess the fitting accuracy between the proposed parametric approximation and the (target) BEM-based system,

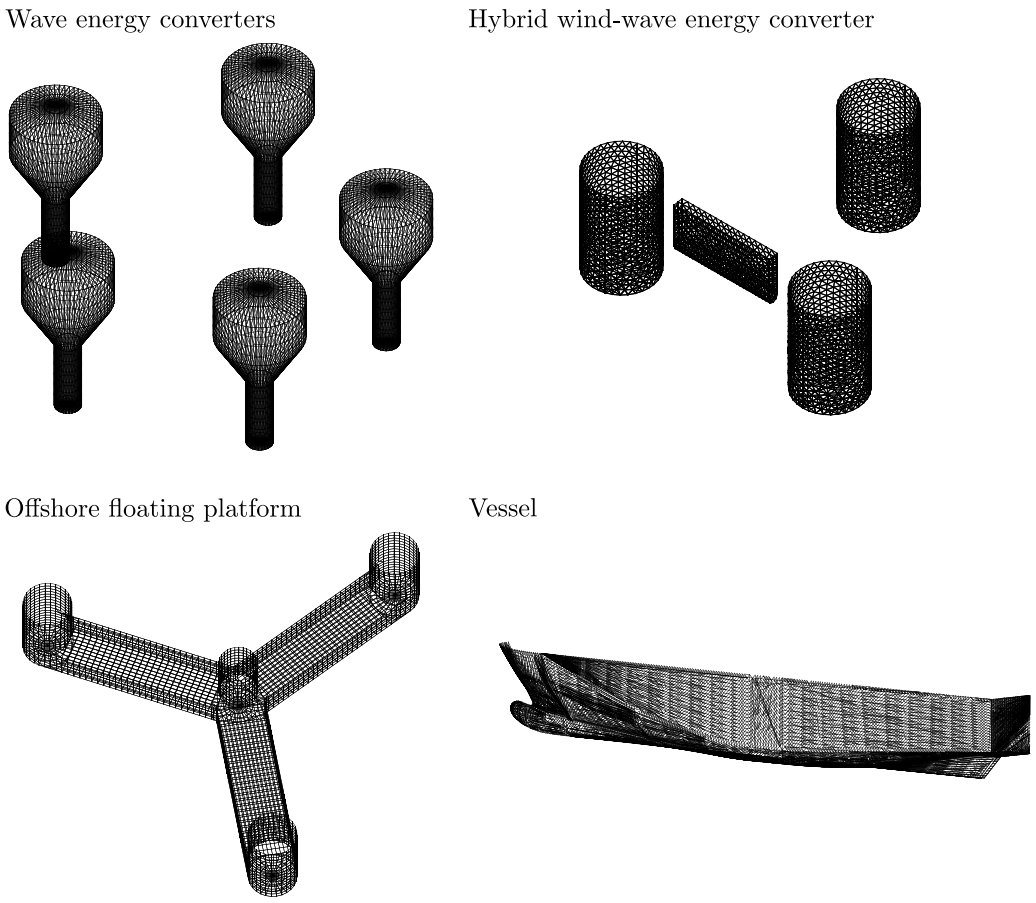

Fig. 4. Surface mesh used for the hydrodynamic solver for the analysed case studies.

Table 1
Main dimensions and associated DoFs for each of the analysed case studies.

Case study	Main dimensions	[m]	DoFs	m
Large Vessel	Length	170	Roll	1
	Draft	20		
	Width	30		
WECs	Diameter	8.4	Heave for each WEC	5
	Draft	14.5		
Offshore wind platform	Draft	20	Heave and pitch	2
	Fairlead radius	51.8		
HWWEC	Flap width	1.5	Pitch (flap) - surge and pitch (platform)	3
	Flap length	15		
	Flap draft	7.5		
	Platform cylinder radius	5		
	Platform draft	16		

we leverage system-oriented error indices. In particular, the frequency-domain approximation errors between the passivised Loewner-based model and the reference hydrodynamic data are measured in terms of both $\mathcal{H}_\infty$- and $\mathcal{H}_2$-errors, defined as:

$$\begin{aligned}\mathcal{H}_\infty\text{-error} &= \frac{\max_{i\in\mathbb{N}_u}\sigma_1(\tilde{K}_{\text{pas}}(j\omega_i) - K(j\omega_i))}{\max_{i\in\mathbb{N}_u}\sigma_1(K(j\omega_i))},\\ \mathcal{H}_2\text{-error} &= \sqrt{\frac{\sum_{i\in\mathbb{N}_u}\|\tilde{K}_{\text{pas}}(j\omega_i) - K(j\omega_i)\|_F^2}{\sum_{i\in\mathbb{N}_u}\|K(j\omega_i)\|_F^2}},\end{aligned} \tag{30}$$

where $\sigma_1(\cdot)$ represents the largest singular value. The former error measure evaluates the maximum deviation in the singular values of $\tilde{K}_{\text{pas}}$ on the imaginary axis, while the latter evaluates the error in the magnitude of all entries, providing an estimate of the overall performance of the model.

Before introducing and discussing each specific case study, Table 2 offers the reader an overview of the computed errors in both norms, along with the resulting model order n for each case study. The latter is selected based on a predefined threshold on the singular value decomposition of the Loewner pencil, ensuring stability and balancing accuracy and complexity. Simpler systems (geometries), such as the large vessel, exhibit lower approximation errors with relatively lower model orders compared to more complex geometries, such as the array of WECs, which naturally requires a higher-order parametric model to represent accurately the underpinning dynamical behaviour. The table also reports the frequency range, Ω, employed for the identification,

Table 2
$\mathcal{H}_\infty$ and $\mathcal{H}_2$ errors between the passivised parametric approximation model and the BEM-based hydrodynamic data for each case study, together with the corresponding model order n and the frequency range Ω used for the identification.

Case study	$\mathcal{H}_\infty$-error	$\mathcal{H}_2$-error	n	Ω [rad/s]
Large vessel	0.0059	0.0838	9	[0.1, 3]
WECs	0.0818	0.1001	101	[0.4, 4]
Wind platform	0.0007	0.0321	25	[0.4, 3]
HWWEC	0.0771	0.1862	23	[0.2, 3]

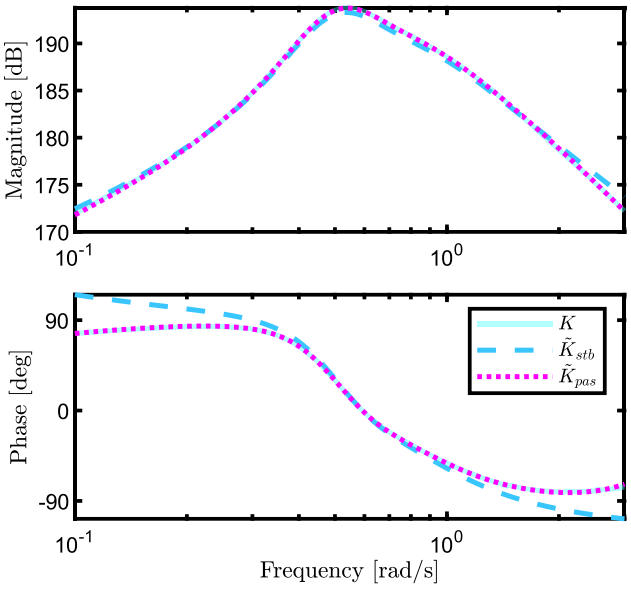

Fig. 5. Large vessel: Bode plot comparison between the BEM-based system K, the stable approximant $\tilde{K}_{\text{stb}}$, and the passivised model $\tilde{K}_{\text{pas}}$.

which is tailored to each case study to capture the most relevant dynamics within the operational bandwidth of interest.

5.1. Large vessel

The first analysed case study is a large vessel, previously studied in Tuzcu et al. (2021), with geometric characteristics detailed in Peña-Sanchez et al. (2019). The numerical model considered in the following represents the vessel dynamics through a single DoF, corresponding to motion in roll. A visual representation of the computational mesh used for the hydrodynamic analysis is provided in Fig. 4 (lower right corner).

This system serves as a relatively simple (in terms of geometry) test case, suitable for evaluating the fundamental accuracy and stability of the proposed parametric approximation. The following analysis focuses on comparing the BEM-derived hydrodynamic response with the Loewner-based models in the frequency domain. In particular, Fig. 5 presents a Bode plot comparing the target numerically derived (BEM) system, K, the stable interpolant, $\tilde{K}_{\text{stb}}$, and its passivised version, $\tilde{K}_{\text{pas}}$.

The approximation shows good overall agreement across the full frequency range. While the stable model $\tilde{K}_{\text{stb}}$ exhibits slight discrepancies at both lower and higher frequencies, particularly in phase, these are effectively corrected after passivity enforcement, via the convex semi-definite formulation in (29). The passivised model $\tilde{K}_{\text{pas}}$ achieves an almost perfect match with the target reference BEM data, both in magnitude and phase, highlighting the robustness of the approximation and passivation procedures. Fig. 6 further illustrates the behaviour of the approximated model by comparing the radiation damping and radiation added mass curves, computed with BEM codes, and $\tilde{K}_{\text{pas}}$, by simply leveraging Eq. (5). Consistent with the Bode plot in Fig. 5,

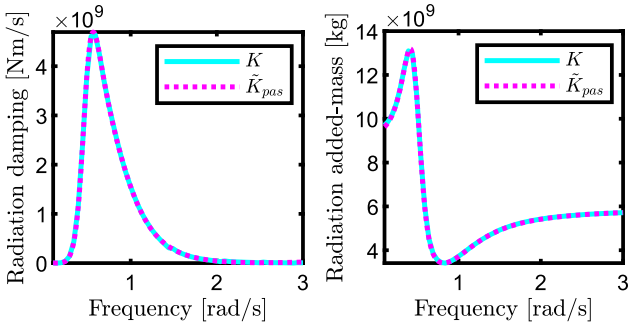

Fig. 6. Large vessel: Radiation damping and added-mass of the target model, K, and its passivised approximated version, $\tilde{K}_{\text{pas}}$.

the passivised model closely follows the original curves across the full frequency spectrum, indicating accurate preservation of hydrodynamic characteristics in the parametric approximate description with passivity enforcement.

5.2. Wave energy converters

The second case study concerns an array of heaving point-absorber type WECs based on the CorPower design. The system consists of five identical devices arranged in a polytopic configuration, as detailed in Faedo et al. (2021b), where further details on device dimensions and array layout can be found. Each device is modelled with a single degree of freedom corresponding to heave motion, resulting in an overall MIMO system with a total of five DoFs, *i.e.* $m = 5$. Unlike the single-body case, WEC arrays are subject to complex hydrodynamic interactions, including coupling effects among each unit (Folley, 2016). These interactions significantly influence the system dynamics and are often described in terms of higher-order behaviour.

We begin by assessing compliance with passivity. To achieve this, Fig. 7 provides an appraisal of the frequency-dependent function

$$\mathcal{P}(\omega) = \min \lambda \left(K(\jmath\omega) + K(\jmath\omega)^\star \right), \tag{31}$$

i.e. the minimum eigenvalue characterising the Hermitian part of $K(\jmath\omega)$. In other words, the map $\mathcal{P}$ represents the sign of the Hermitian part of $K(\jmath\omega)$ which, if the system under analysis is effectively passive, must be non-negative for all $\omega \in \mathbb{R}$. As can be appreciated in Fig. 7, the stable approximant $\tilde{K}_{\text{stb}}$ violates this condition in several frequency intervals, indicated by portions of the curve that fall within the shaded (non-passive) region. In particular, notable passivity violations occur at both low and high frequencies, as highlighted in the two insets. After enforcing passivity, the corresponding model $\tilde{K}_{\text{pas}}$ yields a curve that remains entirely outside the grey area, indicating a non-negative Hermitian part of the system across the entire spectrum. This demonstrates the effectiveness of the passivisation procedure in restoring (P3) without compromising approximation quality. To further validate this, Fig. 8 presents the sigma plot comparing the target system, K, with the parametric stable approximation, $\tilde{K}_{\text{stb}}$ and its passivised counterpart, $\tilde{K}_{\text{pas}}$.

The two models show excellent agreement across the frequency range with respect to the target BEM response, with a nearly perfect superposition on the dominant (highest) singular value curve. Minor deviations can be observed at lower frequencies, particularly in the passivised approximation, though these differences remain small. This indicates that the passivisation procedure preserves the overall dynamic behaviour effectively, thereby achieving both physical consistency and accurate approximation.

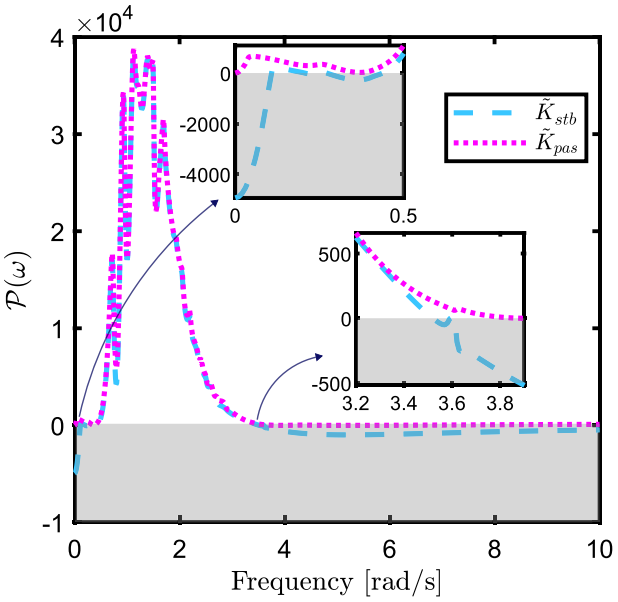

Fig. 7. Wave energy converters: Graphical appraisal of the map $\mathcal{P}(\omega)$ for both $\tilde{K}_{\text{stb}}$ and passivised counterpart $\tilde{K}_{\text{pas}}$. The non-passivity boundary is indicated using a grey area.

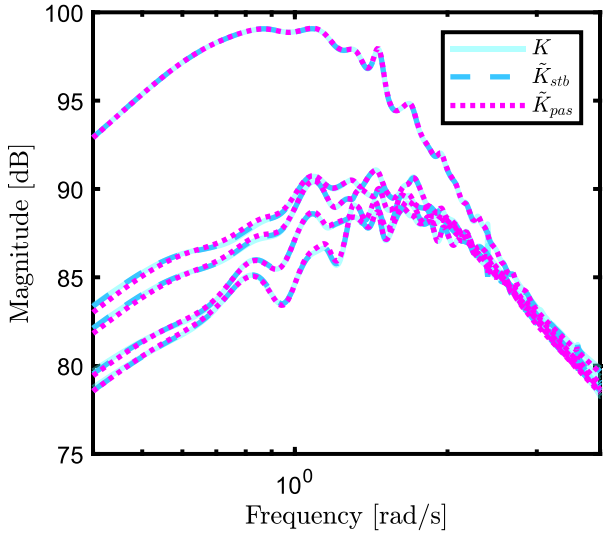

Fig. 8. Wave energy converters: Sigma plot comparison between the BEM reference model, K, the parametric approximation, $\tilde{K}_{\text{stb}}$, and its passivised counterpart, $\tilde{K}_{\text{pas}}$.

5.3. Offshore wind platform

In this section, a floating offshore wind platform with a semi-submersible configuration is considered. Detailed geometric specifications are available in Allen et al. (2020), with a summary of the main parameters reported in Table 1. The hydrodynamic mesh used for the BEM analysis is shown in Fig. 4. The platform dynamics are modelled in two DoFs, *i.e.* heave and pitch. In this case study, both frequency and time-domain analyses are performed. As shown in Fig. 9, the Bode diagram reveals an excellent match between the original BEM-based hydrodynamic operator and the approximated system.

The fitting quality is evident not only in the diagonal terms, representing the direct response in heave and pitch, but also in the off-diagonal components, which capture the coupling between the two modes of motion. This highlights the ability of the parametric model, both in its stabilised and passivised versions, to replicate the behaviour of the original BEM-based system accurately. The passivised system, $\tilde{K}$pas, does not introduce notable distortions with respect to the stable approximation, as demonstrated by the near-perfect overlap both in magnitude and phase responses across all input–output pairs. Therefore, the passivisation step, necessary to restore the physical coherence of the operator, does not compromise the fidelity of the model.

The validity of the approximation is further confirmed in the time domain. In particular, Fig. 10 presents the impulse response associated with the target radiation system, k in (1), and the proposed approximation, $\tilde{k}_{\text{pas}}$ in (28). The parametric model response presents an almost perfect overlap with the target impulse response across all input–output channels, confirming the accuracy of the parametric model in capturing the underlying radiation dynamics, further validating the quality and reliability of the proposed Loewner-based approximation.

5.4. Hybrid wind-wave energy converter

Within this section, a hybrid wind-wave energy converter (HWWEC) is analysed. In particular, the benchmark concept presented in Celesti et al. (2023) is adopted, and its corresponding hydrodynamic panel mesh is illustrated herein in Fig. 4. The device consists of a semisubmersible triangular floating offshore wind platform, with a rectangular flap-type wave energy converter hinged to the structure. The overall hybrid device is represented in terms of three DoFs, *i.e.* pitch of the WEC, and pitch and surge of the platform.

Within this case study, we analyse the effect of radiation forces on the overall force-to-velocity mapping, *i.e.* the map $f_e \mapsto \dot{q}$. Results are presented in both the frequency and time domains. In particular, as shown in Fig. 11, the Bode diagram of the input/output (I/O) response $f_e \mapsto \dot{q}$ highlights the dynamic behaviour of the HWWEC across its three considered DoFs, comparing the I/O response obtained using the target hydrodynamic operator, K, its stable approximation $\tilde{K}_{\text{stb}}$, and the passivised version $\tilde{K}_{\text{pas}}$.

The approximation accurately captures both the magnitude and phase trends of the frequency response, with a particularly good match within the frequency range used for the identification (white area). Only minor deviations are observed outside the identification range (grey-shaded regions), mainly affecting the off-diagonal terms, while the dominant dynamics are well captured across the entire frequency span considered in the I/O response.

Compared to the stand-alone platform (analysed in Section 5.3), the HWWEC system exhibits more complex dynamics due to the additional DoF introduced by the WEC and its coupling with the platform motion. Despite this increased complexity, the structure of the interactions among the different DoFs is well reproduced by the proposed Loewner-based procedure. This is particularly evident in the off-diagonal terms, which are well approximated despite featuring more pronounced modes (peaks) and phase variations, as a result of the flap-platform coupling. These results further confirm the effectiveness of the proposed parametric model in accurately representing even more intricate hydrodynamic configurations.

To finalise with the presented results, we analyse the I/O behaviour for the case in which the parametric approximation is stable, *i.e.* $\tilde{K}_{\text{stb}}$, and for that in which the passivised counterpart is considered, *i.e.* $\tilde{K}_{\text{pas}}$. In particular, the aim is to assess whether the stable approximation, $\tilde{K}_{\text{stb}}$, also ensures a physically consistent input/output behaviour. To this end, a pole-zero map is presented in Fig. 12, comparing the force-to-motion (velocity) response for the stable approximation with its passivised counterpart, $\tilde{K}_{\text{pas}}$. Poles and zeros are indicated with crosses and circles, respectively. While both radiation approximants are stable per se, *i.e.* all poles have negative real parts, when considering the I/O behaviour, this property is not necessarily guaranteed. The zoomed-in view, in fact, highlights a critical detail: the I/O system with a parametric radiation system $\tilde{K}_{\text{stb}}$ exhibits a pole on the right side of

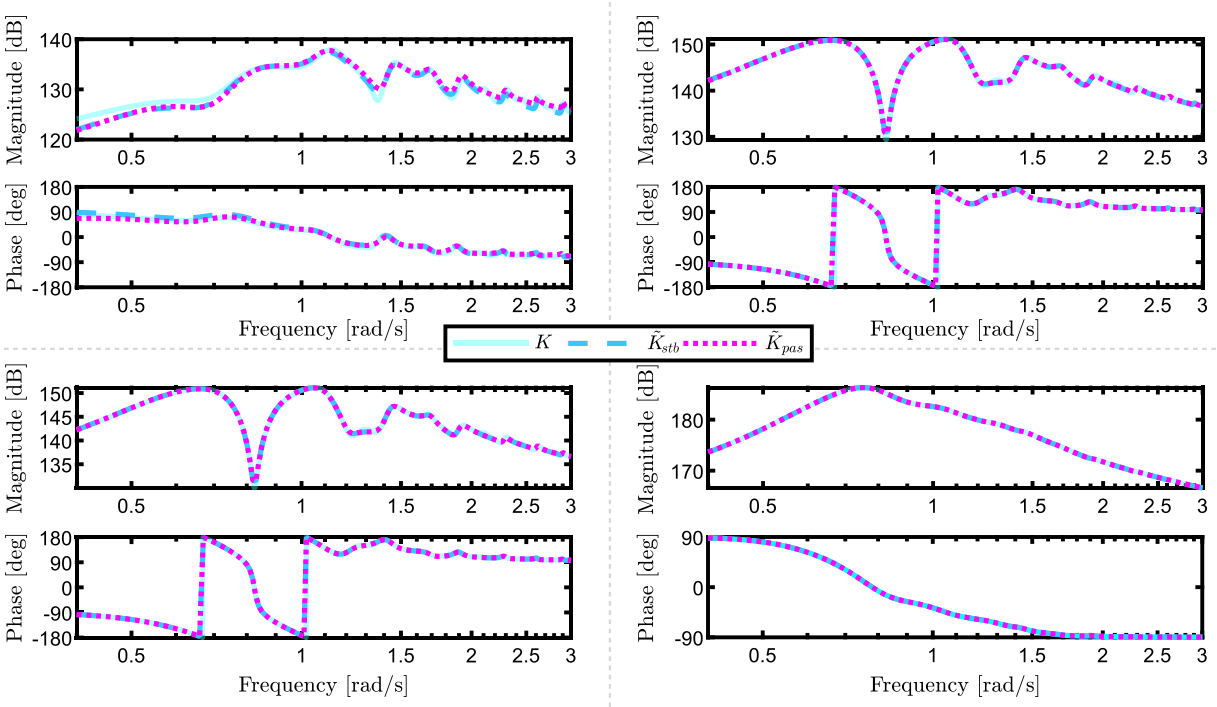

Fig. 9. Offshore wind platform: Bode plot for the frequency response of the radiation system, computed via BEM solver K, obtained stable approximation K_{stb} and passivised system K_{pas}.

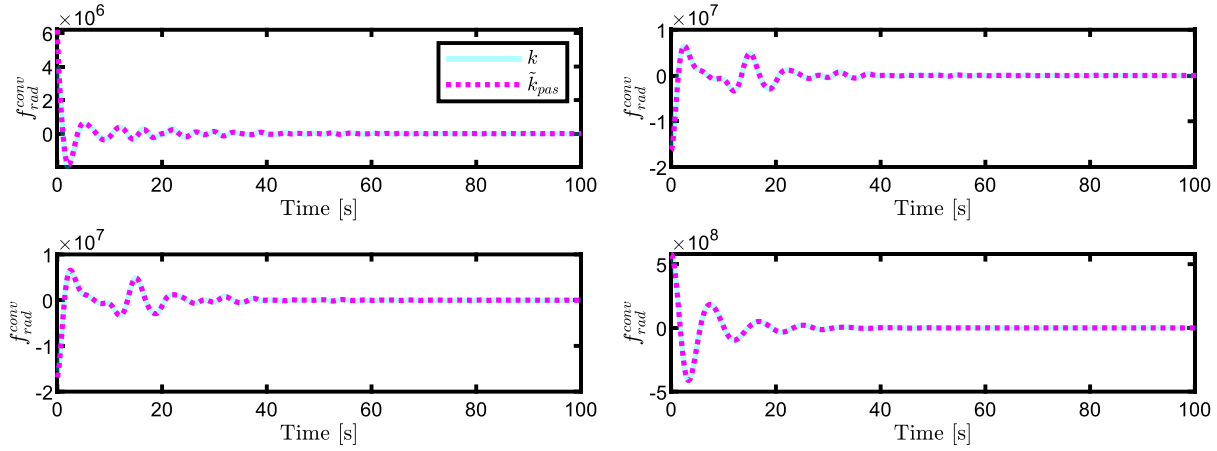

Fig. 10. Offshore wind platform: Impulse response function of the target k and passivised approximating $\tilde{k}_{\text{pas}}$ radiation impulse response function.

the complex plane, *i.e.* grey-shaded area, resulting in a violation of input/output stability. This confirms that, although $\tilde{K}$stb is asymptotically stable, it fails to guarantee this requirement in the overall Eq. (1). On the other hand, the passivised model $\tilde{K}$pas guarantees I/O stability by virtue of the passive behaviour itself, as discussed within Section 2. This highlights the practical importance of the passivisation step in obtaining a reliable approximation and a model suitable for simulation/optimisation/control purposes.

Finally, to validate the I/O approximation quality in the time domain, a simulation under realistic excitation is performed. Fig. 13 presents the velocity response of the hybrid system to a specific excitation signal f_{e}, derived from irregular waves. The comparison involves the non-parametric BEM-based radiation kernel, k (solid line), computed using an explicit discretisation of the corresponding convolution operators, and its passivised parametric approximation $\tilde{k}_{\text{pas}}$ (dashed line). For reference, the force input is also provided in the figure. The responses are shown for all three DoFs and reveal a remarkable agreement between the two models. The velocity traces produced by the I/O model considering $\tilde{k}_{\text{pas}}$ closely follow the target response across the entire simulation window, even in the presence of complex interactions. This result confirms that the proposed Loewner-based passive approximation produces highly accurate models, while ensuring input/output stability, a crucial requirement for a consistent representation of time-domain behaviour.

6. Conclusions

This paper presents a novel parameterisation technique for physically consistent time-domain modelling of floating offshore structures. We leverage the concept of Loewner matrices and provide a robust methodology to produce state-space models from raw frequency-domain data provided by standard BEM hydrodynamic solvers. Furthermore, tailored strategies to ensure stability and passivity (and hence also minimum-phase behaviour), intrinsic to radiation effects, are

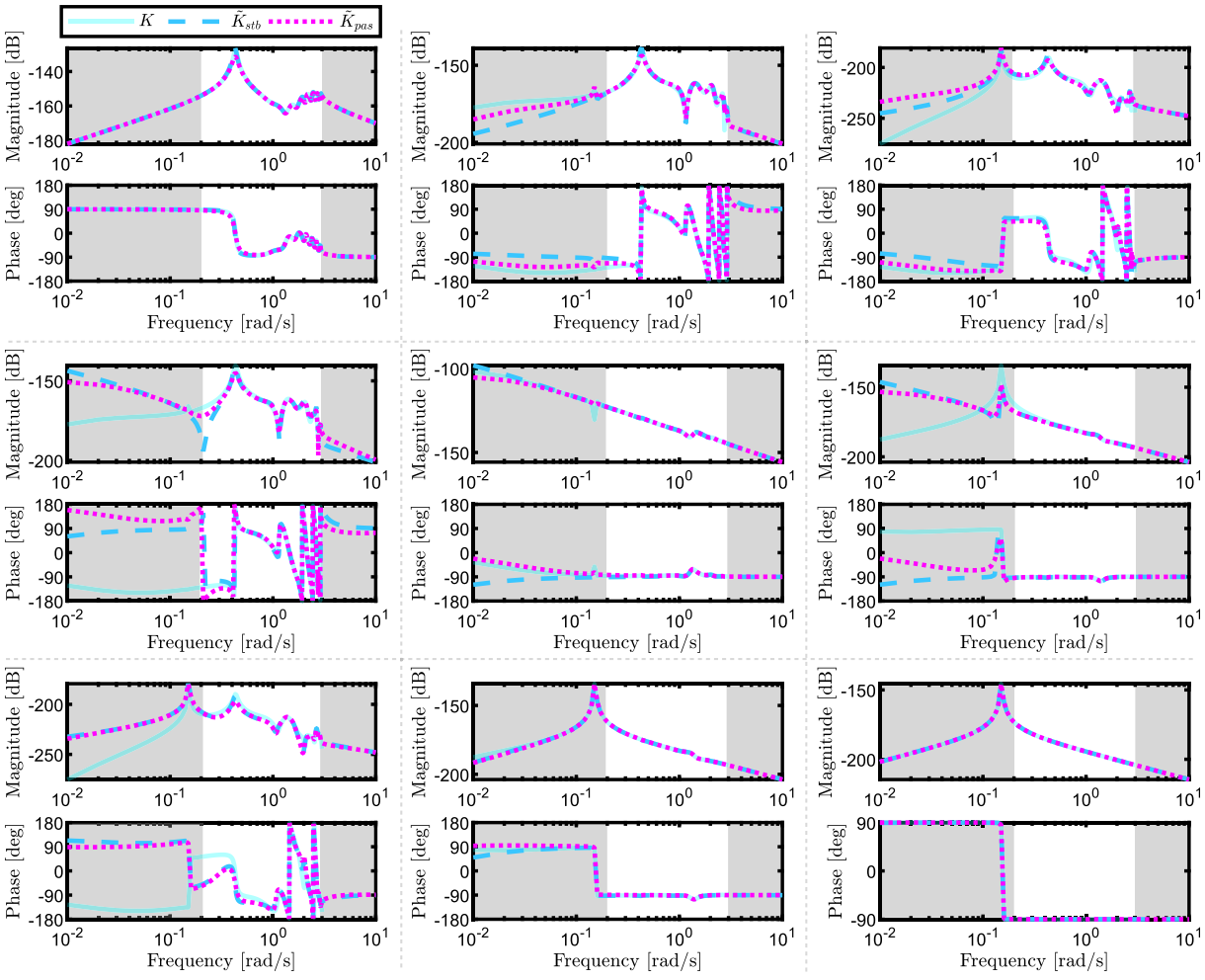

Fig. 11. Hybrid wind-wave energy converter: Bode of the input/output response. The white area indicates the frequency range used for the identification.

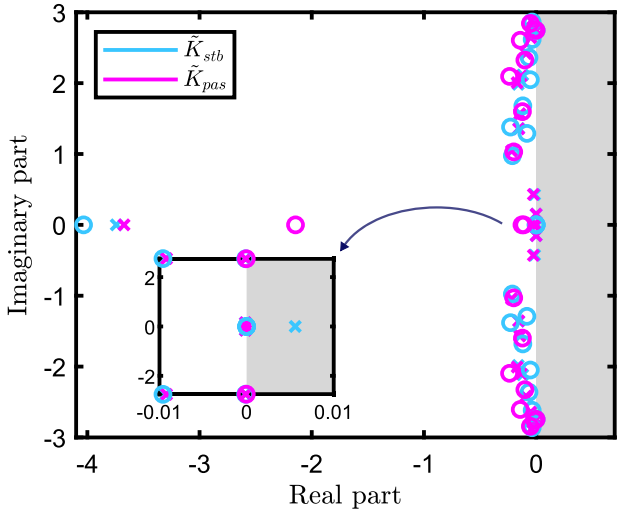

Fig. 12. Hybrid wind-wave energy converter: Pole-zero map of the input/output response considering the approximating stable system $\tilde{K}_{\text{stb}}$ and the corresponding passivised counterpart $\tilde{K}_{\text{pas}}$.

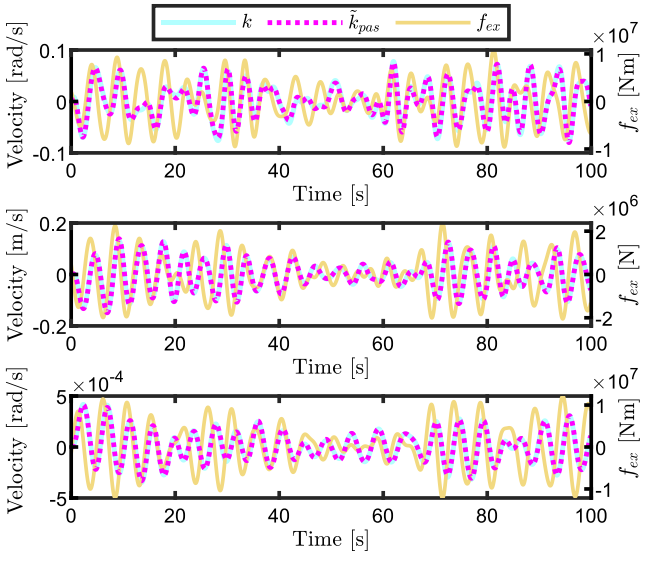

Fig. 13. Hybrid wind-wave energy converter: Time-domain comparison of velocity, computed using the non-parametric BEM-based kernel (solid line) and its parametric approximation (dashed line). The same force f_{e} (right axis) is used as input to both models.

devised and incorporated accordingly, via linear operations and convex semi-definite optimisation, respectively. The overall technique is illustrated using four different floating offshore structures, featuring multi-DoF and multi-body behaviour. Via a detailed numerical appraisal, we show that the proposed parameterisation technique produces models with remarkable accuracy for all the considered structures, being intrinsically able to guarantee all physical properties underpinning generic floating devices. This provides the ocean and marine engineering community with an accurate and robust solution to produce time-domain hydrodynamic models for generic complex floating structures, being this a fundamental tool to design, optimise, and control existing and novel marine systems. Future work will include a detailed comparison of the proposed parameterisation technique against benchmark strategies.

CRediT authorship contribution statement

Maria Luisa Celesti: Writing – review & editing, Writing – original draft, Visualization, Validation, Software, Methodology, Formal analysis, Data curation, Conceptualization. **Nicolás Faedo:** Writing – review & editing, Writing – original draft, Visualization, Validation, Supervision, Software, Resources, Project administration, Methodology, Investigation, Funding acquisition, Formal analysis, Data curation, Conceptualization.

Declaration of competing interest

The authors declare that they have no known competing financial interests or personal relationships that could have appeared to influence the work reported in this paper.

Acknowledgements

Project funded by the European Union - NextGenerationEU under the National Recovery and Resilience Plan (NRRP), Mission 4 Component 2 Investment 1.2 | Project code: MSCA2024_0000032 - CUP: E13C25001010006 – Project title: Unlocking wave power: Economic-aware control co-design for wave energy conversion (ECOWAVE).

References

Allen, Christopher, Viscelli, Anthony, Dagher, Habib, Goupee, Andrew, Gaertner, Evan, Abbas, Nikhar, Hall, Matthew, Barter, Garrett, 2020. Definition of the UMaine VolturnUS-S reference platform developed for the IEA wind 15-megawatt offshore reference wind turbine. Technical report, National Renewable Energy Lab. (NREL), Golden, CO (United States); Univ. of Maine.

Ancellin, Matthieu, Dias, Frédéric, 2019. Capytaine: a python-based linear potential flow solver. J. Open Source Softw. 4 (36), 1341.

Antoulas, Athanasios C, Lefteriu, Sanda, Ionita, A Cosmin, Benner, P, Cohen, A, 2017. A tutorial introduction to the loewner framework for model reduction. Model. Reduct. Approx.: Theory Algorithms 15, 335.

Armesto, José A, Guanche, Raúl, Jesus, Fernando del, Iturrioz, Arantza, Losada, Iñigo J, 2015. Comparative analysis of the methods to compute the radiation term in cummins' equation. J. Ocean. Eng. Mar. Energy 1 (4), 377–393.

Astolfi, Alessandro, 2010. Model reduction by moment matching for linear and nonlinear systems. IEEE Trans. Autom. Control 55 (10), 2321–2336.

Astolfi, Alessandro, Scarciotti, Giordano, Simard, Joel, Faedo, Nicolás, Ringwood, John V, 2020. Model reduction by moment matching: Beyond linearity a review of the last 10 years. In: 2020 59th IEEE Conference on Decision and Control. CDC, IEEE, pp. 1–16.

Bavely, Connice A., Stewart, G.W., 1979. An algorithm for computing reducing subspaces by block diagonalization. SIAM J. Numer. Anal. 16 (2), 359–367.

Carapellese, Fabio, Paduano, Bruno, Faedo, Nicolás, et al., 2024. Performance optimisation of wave energy converters. Ref. Modul. Earth Syst. Environ. Sci..

Celesti, Maria Luisa, Mattiazzo, Giuliana, Faedo, Nicolás, 2025. Towards modelling and control strategies for hybrid wind-wave energy converters: Challenges and opportunities. Renew. Sustain. Energy Rev. 224, 116080.

Celesti, Maria Luisa, Paduano, Bruno, Peña-Sanchez, Yerai, Pasta, Edoardo, Faedo, Nicolás, Ringwood, John V, 2023. On the behaviour of a combined wind-wave energy conversion platform under energy-maximising control conditions. In: OCEANS 2023-Limerick. IEEE, pp. 1–6.

Cummins, W.E., 1962. The impulse response function and ship motions. Schiffstechnik. Heft 47, 101–109.

Faedo, Nicolás, Peña-Sanchez, Yerai, Carapellese, Fabio, Mattiazzo, Giuliana, Ringwood, John V, 2021a. LMI-based passivation of LTI systems with application to marine structures. IET Renew. Power Gener. 15 (14), 3424–3433.

Faedo, Nicolás, Peña-Sanchez, Yerai, García-Violini, Demián, Ferri, Francesco, Mattiazzo, Giuliana, Ringwood, John V, 2023. Experimental assessment and validation of energy-maximising moment-based optimal control for a prototype wave energy converter. Control Eng. Pract. 133, 105454.

Faedo, Nicolás, Peña-Sanchez, Yerai, Ringwood, John V., 2018a. Finite-order hydrodynamic model determination for wave energy applications using moment-matching. Ocean Eng. 163, 251–263.

Faedo, Nicolás, Peña-Sanchez, Yerai, Ringwood, John V., 2018b. Passivity preserving moment-based finite-order hydrodynamic model identification for wave energy applications. In: Advances in Renewable Energies Offshore, RENEW, vol. 2018, pp. 351–359.

Faedo, Nicolás, Peña-Sanchez, Yerai, Ringwood, John V., 2020. Parametric representation of arrays of wave energy converters for motion simulation and unknown input estimation: a moment-based approach. Appl. Ocean Res. 98, 102055.

Faedo, Nicolás, Scarciotti, Giordano, Astolfi, Alessandro, Ringwood, John V, 2021b. Energy-maximising moment-based constrained optimal control of ocean wave energy farms. IET Renew. Power Gener. 15 (14), 3395–3408.

Falnes, Johannes, Kurniawan, Adi, 2020. Ocean Waves and Oscillating Systems: Linear Interactions Including Wave-Energy Extraction. vol. 8, Cambridge University Press.

Faltinsen, Odd, 1993. Sea Loads on Ships and Offshore Structures. vol. 1, Cambridge University Press.

Folley, Matt, 2016. Numerical Modelling of Wave Energy Converters: State-Of-The-Art Techniques for Single Devices and Arrays. Academic Press.

Folley, Matt, Babarit, Aurélien, Child, Ben, Forehand, David, O'Boyle, Louise, Silverthorne, Katie, Spinneken, Johannes, Stratigaki, Vasiliki, Troch, Peter, 2012. A review of numerical modelling of wave energy converter arrays. In: International Conference on Offshore Mechanics and Arctic Engineering. vol. 44946, American Society of Mechanical Engineers, pp. 535–545.

Fossen, Thor I., 2011. Handbook of marine craft hydrodynamics and motion control. John Wiley & Sons.

Husain, Salman, Parker, Gordon G, Forehand, David, Anderlini, Enrico, 2023. Radiation force modeling for a wave energy converter array. Energies 17 (1), 6.

IRENA, 2020. Innovation Outlook: Ocean Energy Technologies. Technical report, International Renewable Energy Agency.

Karachalios, Dimitrios, Gosea, Ion Victor, Antoulas, Athanasios C, 2021. The loewner framework for system identification and reduction. In: Model Order Reduction: Volume I: System-and Data-Driven Methods and Algorithms. de Gruyter, pp. 181–228.

Kergus, Pauline, Gosea, Ion Victor, 2022. Data-driven approximation and reduction from noisy data in matrix pencils frameworks. IFAC-PapersOnLine 55 (30), 371–376.

Köhler, M., 2014. On the closest stable descriptor system in the respective spaces RH_2 and RH_∞. Linear Algebra Appl. 443, 34–49.

Kristiansen, Erlend, Hjulstad, Åsmund, Egeland, Olav, 2005. State-space representation of radiation forces in time-domain vessel models. Ocean Eng. 32 (17–18), 2195–2216.

Kundu, Pijush K, Cohen, Ira M, Dowling, David R, Capecelatro, Jesse, 2024. Fluid Mechanics. Elsevier.

Lee, Hye-Won, Roh, Myung-Il, 2018. Review of the multibody dynamics in the applications of ships and offshore structures. Ocean Eng. 167, 65–76.

Löfberg, J., 2004. YALMIP: A toolbox for modeling and optimization in MATLAB. In: In Proceedings of the CACSD Conference. Taipei, Taiwan.

Marquez, Horacio J., 2003. Nonlinear Control Systems: Analysis and Design. vol. 161, John Wiley Hoboken^ eN. JNJ.

Mayo, A.J., Antoulas, Athanasios C., 2007. A framework for the solution of the generalized realization problem. Linear Algebra Appl. 425 (2–3), 634–662.

MOSEK ApS, 2025. MOSEK optimization suite. URL https://docs.mosek.com/.

Otter, Aldert, Murphy, Jimmy, Pakrashi, Vikram, Robertson, Amy, Desmond, Cian, 2022. A review of modelling techniques for floating offshore wind turbines. Wind. Energy 25 (5), 831–857.

Papillon, Louis, Costello, Ronan, Ringwood, John V., 2020. Boundary element and integral methods in potential flow theory: A review with a focus on wave energy applications. J. Ocean. Eng. Mar. Energy 6, 303–337.

Peña-Sanchez, Yerai, Faedo, Nicolás, Ringwood, John V., 2019. A critical comparison between parametric approximation methods for radiation forces in wave energy systems. In: ISOPE International Ocean and Polar Engineering Conference. ISOPE, pp. ISOPE–I.

Perez, Tristan, Fossen, Thor I., 2009. A matlab toolbox for parametric identification of radiation-force models of ships and offshore structures. Model. Identif. Control. 30.

Perez, Tristan, Fossen, Thor I., 2011. Practical aspects of frequency-domain identification of dynamic models of marine structures from hydrodynamic data. Ocean Eng. 38 (2–3), 426–435.

Ringwood, John V., Zhan, Siyuan, Faedo, Nicolás, 2023. Empowering wave energy with control technology: Possibilities and pitfalls. Annu. Rev. Control..

Sahoo, Avilash, Dwivedy, Santosha K., Robi, P.S., 2019. Advancements in the field of autonomous underwater vehicle. Ocean Eng. 181, 145–160.

Sturm, Jos F., 1999. Using SeDuMi 1.02, a MATLAB toolbox for optimization over symmetric cones. Optim. Methods Softw. 11 (1–4), 625–653.

Taghipour, Reza, Perez, Tristan, Moan, Torgeir, 2008. Hybrid frequency–time domain models for dynamic response analysis of marine structures. Ocean Eng. 35 (7), 685–705.

Tuzcu, Cantekin, Dinsdale, Cameron, Hawkins, Jack, Zaraphonitis, George, Papadopoulos, Fotis, 2021. Ropax design revisited—Evolution or revolution? In: A Holistic Approach To Ship Design: Volume 2: Application Case Studies. Springer, pp. 327–371.

Unneland, Kari, Egeland, Olav, 2006. Positive real modeling of ships for dynamic positioning. In: In Proc. of 17th International Symposium on Mathematical Theory of Networks and Systems. July 24-28, Kyoto, Japan.

White, F.M., 2011. Fluid Mechanics. In: McGraw-Hill Series in Mechanical Engineering, McGraw Hill.

Wilson, James F., 2003. Dynamics of Offshore Structures. John Wiley & Sons.

Zabala, I, Henriques, JCC, Kelly, TE, Ricci, PP, Blanco, JM, 2024. Post-processing techniques to improve the results of hydrodynamic boundary element method solvers. Ocean Eng. 295, 116913.

Zereik, Enrica, Bibuli, Marco, Mišković, Nikola, Ridao, Pere, Pascoal, António, 2018. Challenges and future trends in marine robotics. Annu. Rev. Control. 46, 350–368.